JACS
JOURNAL OF THE AMERICAN CHEMICAL SOCIETY
Article
pubs.acs.org/JACS

Ultrastable Polymolybdate-Based Metal–Organic Frameworks as Highly Active Electrocatalysts for Hydrogen Generation from Water

Jun-Sheng Qin,[†,§] Dong-Ying Du,[†] Wei Guan,[†] Xiang-Jie Bo,[†] Ya-Fei Li,[‡] Li-Ping Guo,[†] Zhong-Min Su,*[,†] Yuan-Yuan Wang,[†] Ya-Qian Lan,*[,†,‡] and Hong-Cai Zhou*[,§]

[†]Institute of Functional Material Chemistry, Key Lab of Polyoxometalate Science of Ministry of Education, Department of Chemistry, Northeast Normal University, Changchun 130024, P. R. China

[‡]School of Chemistry and Materials Science, Nanjing Normal University, Nanjing 210046, P. R. China

[§]Department of Chemistry, Texas A&M University, College Station, Texas 77843-3255, United States

Supporting Information

ABSTRACT: Two novel polyoxometalate (POM)-based metal–organic frameworks (MOFs), $[TBA]_3[\varepsilon\text{-}PMo^{V}_{8}Mo^{VI}_{4}O_{36}(OH)_4Zn_4][BTB]_{4/3}\cdot x$Guest (**NENU-500**, BTB = benzene tribenzoate, TBA^+ = tetrabutylammonium ion) and $[TBA]_3[\varepsilon\text{-}PMo^{V}_{8}Mo^{VI}_{4}O_{37}(OH)_3Zn_4][BPT]$ (**NENU-501**, BPT = [1,1′-biphenyl]-3,4′,5-tricarboxylate), were isolated. In these compounds, the POM fragments serving as nodes were directly connected with organic ligands giving rise to three-dimensional (3D) open frameworks. The two anionic frameworks were balanced by TBA^+ ions residing inside the open channels. They exhibit not only good stability in air but also tolerance to acidic and basic media. Furthermore, they were employed as electrocatalysts for the hydrogen evolution reaction (HER) owing to the combination of the redox activity of a POM unit and the porosity of a MOF. Meanwhile, the HER activities of $\boldsymbol{\varepsilon}(\mathbf{trim})_{4/3}$, **NENU-5**, and **HKUST-1** were also studied for comparison. Remarkably, as a 3D hydrogen-evolving cathode operating in acidic electrolytes, **NENU-500** exhibits the highest activity among all MOF materials. It shows an onset overpotential of 180 mV and a Tafel slope of 96 mV·dec^{-1}, and the catalytic current density can approach 10 mA·cm^{-2} at an overpotential of 237 mV. Moreover, **NENU-500** and **NENU-501** maintain their electrocatalytic activities after 2000 cycles.

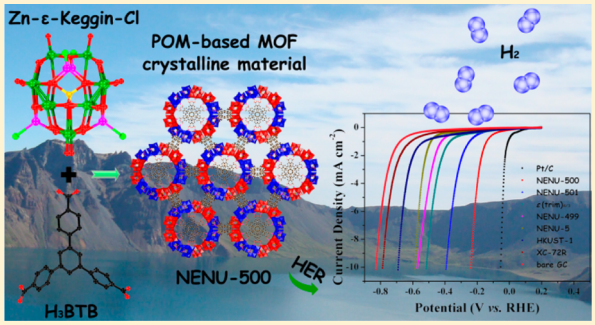

INTRODUCTION

Hydrogen is a potential clean and renewable alternative for fossil fuels in the future.[1] Electrocatalytic reduction of water to molecular hydrogen via hydrogen evolution reaction (HER) may provide a simple but efficient solution to future energy demands. To attain high current density at low overpotential for practical applications, the HER always requires efficient electrocatalysts owing to the multielectron nature of dihydrogen generation through proton reduction.[2] Pioneering studies have demonstrated that Pt-group metals are currently the best HER catalysts,[3] however, their widespread practical utilization has been hampered by the prohibitive cost and low abundance of these precious metals. As a consequence, the exploitation of inexpensive and effective catalysts is highly desirable to viable water electrolytic systems. In addition, the strongly acidic media in proton-exchange membrane (PEM) technology needs acid-stable catalysts for PEM-based electrolysis units.[4] Tremendous efforts have thus been devoted to developing acid-stable non-noble-metal catalysts to improve their HER activity, and encouraging progress has been achieved in the past few years.[5]

One of the exciting families of such catalysts, molybdenum-based materials including MoS_2 and Mo_2C,[6] has been a great success owing to their similar electronic structures to that of noble metals. Moreover, catalysts with permanent porosity are favorable for enhanced HER activity.[7] Therefore, the design and preparation of active, selective, environmentally benign, and recyclable porous non-noble-metal-based catalysts toward HER are expected to have a significant impact on practical applications.

Polyoxometalate (POM) ions, which represent a well-defined library of inorganic building blocks of nanoscopic scale with oxygen-rich surfaces, are ideal candidates for the design and construction of tailored framework materials.[8] Additionally, POMs with redox activity show great promise as redox catalysts for many organic transformations.[9] Nevertheless, the applications of pure bulk POMs as solid catalysts are limited because of their significant solubility in reaction media, which leads to poor recyclability due to the disintegration of active sites. To improve the recyclability, POMs were immobilized on Lewis

Received: March 13, 2015
Published: May 1, 2015

ACS Publications © 2015 American Chemical Society

DOI: 10.1021/jacs.5b02688
J. Am. Chem. Soc. 2015, 137, 7169–7177

acidic porous supports (such as zeolites).[9a,b] However, these materials often suffer from difficulties in synthetic control and leaching of POMs from the porous support.

Metal−organic frameworks (MOFs) are a new class of porous materials with fascinating structures and intriguing properties.[10] Although MOFs with desirable proton conductivity were reported, they have rarely been studied as electrocatalysts owing to their low electrical conductivity. However, the permanent porosity and high surface area of MOFs may provide an advantage toward electrocatalytic reactions[11] such as HER and oxygen reduction reaction (ORR). The availability of various building blocks consisting of POM anions and organic linkers (or metal−organic fragments) makes it possible to construct POM-based MOF materials. Thus, combining the advantages of both POMs and MOFs, such materials may exhibit excellent catalytic activity as electrocatalysts or heterogeneous catalysts. Though POM-based MOF materials were extensively studied as catalysts,[12] so far, there are only a few reports on POM-based MOF materials utilized as HER catalysts.[13]

POM-based MOFs combine the redox nature of the POM moiety and the porosity of a MOF, which may favor hydrogen generation as an electrocatalyst. In addition, the stability of HER catalysts in water over a wide range of pH values is critical. Therefore, it is an important and challenging task to explore the appropriate POMs and suitable organic linkers for the preparation of stable crystalline porous POM-based MOF materials as nonprecious-metal-based electrocatalysts.

Various POM-based MOF crystalline materials were reported in the literature, and we classified them into three main forms in our recent review (Figure S1).[12] In the light of the character of HER catalysts, we employ ε-Keggin polymolybdate units capped by four M ions as secondary building blocks (M = Zn^{II} or La^{III}) to obtain MOFs in which POM units and organic fragments were directly connected.[13−15] Particularly, $\{\varepsilon\text{-}PMo^{V}_{8}Mo^{VI}_{4}O_{40}Zn_4\}$ (Zn-ε-Keggin, Figure 1a) stands out for the following considerations: (i) the Zn-ε-Keggin fragment can be generated *in situ* under mild conditions and possesses excellent redox activity on the basis of the Mo element; and (ii) the four exposed Zn^{II} cations are in a regular tetrahedral arrangement, which is identical to those of O atoms in a tetrahedral SiO_4 unit. This arrangement tends to promote the formation of 4-connected 3D MOFs due to its intrinsic nonplanarity.[10d] Recently, we devoted our efforts to isolating a Zn-ε-Keggin fragment and successfully obtaining a $\{[\varepsilon\text{-}PMo^{V}_{8}Mo^{VI}_{4}O_{37}(OH)_3Zn_4]Cl_4\}^{4-}$ unit (abbreviated as Zn-ε-Keggin-Cl), as crystallized in $[TBA]_4[\varepsilon\text{-}PMo^{V}_{8}Mo^{VI}_{4}O_{37}(OH)_3Zn_4]Cl_4$ (**NENU-499**, TBA^+ = tetrabutylammonium ion). Presumably, there are two steps in the one-pot routine: (i) the Zn-ε-Keggin-Cl was formed initially and (ii) chloride ions were substituted by the carboxylate groups of organic ligands. The replacement reaction is supported by DFT calculations. The binding energy (ΔE_b) of POM-based framework was evaluated with chloride or carboxylate group, as shown in Figure S2. The calculated results suggest that the stability enhancement in the presence of carboxylate is attributable to the larger ΔE_b value (see the Table S1). Bearing this in mind, rigid benzene tribenzoate (BTB)[16] and [1,1′-biphenyl]-3,4′,5-tricarboxylate (BPT)[17] were selected to test the theoretical prediction. As expected, two novel 3D open frameworks, $[TBA]_3[\varepsilon\text{-}PMo^{V}_{8}Mo^{VI}_{4}O_{36}(OH)_4Zn_4][BTB]_{4/3}\cdot x$Guest (**NENU-500**) and $[TBA]_3[\varepsilon\text{-}PMo^{V}_{8}Mo^{VI}_{4}O_{37}(OH)_3Zn_4][BPT]$ (**NENU-501**), were isolated and characterized (Figures S3 and S4). Furthermore, the electrocatalytic activities of the as-synthesized **NENU-500** and **NENU-501** toward HER were examined in acidic aqueous solution (0.5 M H_2SO_4). As a novel non-noble-metal HER catalyst in acidic media, **NENU-500** is highly active with a Tafel slope of 96 mV·dec^{-1} and an exchange current density of 0.036 mA·cm^{-2}. It needs an overpotential (η) of 237 mV to attain a current density of 10 mA·cm^{-2}. In addition, the free energy of the Zn-ε-Keggin-Cl unit was studied to evaluate its HER activity by DFT calculations. **NENU-500** and **NENU-501** maintain their activities after 2000 cycles. For comparison, the HER behaviors of commercial Pt/C, $\boldsymbol{\varepsilon}$**(trim)**$_{4/3}$, **NENU-5**, and **HKUST-1** were also examined under similar conditions.

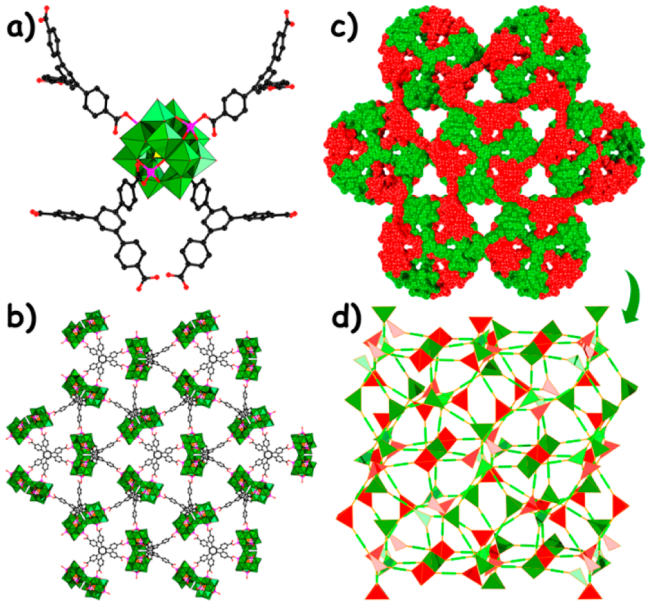

Figure 1. Summary of the structure of **NENU-500**: (a) connection mode between Zn-ε-Keggin and BTB^{3-} fragments, (b) 3D (3,4)-connected framework, (c) two-fold interpenetrated structure, and (d) two-fold interpenetrated **ctn** arrays.

RESULTS AND DISCUSSION

NENU-499. Single-crystal X-ray diffraction analysis demonstrates that **NENU-499** crystallizes in the tetragonal $P\bar{4}2_1c$ space group (Table S2). **NENU-499** comprises a Zn-ε-Keggin-Cl unit and TBA^+ cations (Figure S5). The $\varepsilon\text{-}PMo_{12}O_{40}$ core, initially reported by Sécheresse and co-workers,[14] derives formally from the α-Keggin isomer by rotation of all four Mo_3O_{13} groups by 60° around the C_3 axes (Figure S6). Only ε-Keggin ions capped by La^{3+}, Zn^{2+}, and Ni^{2+} are encountered in the literature;[15] naked ε-Keggin ions have never been isolated, presumably due to their high negative charges. As expected, the ε-Keggin ion is an eight-electron-reduced POM unit, containing eight Mo(V) and four Mo(VI) ions, as indicated by the short Mo(V)−Mo(V) (∼2.6 Å) and long Mo(VI)−Mo(VI) (∼3.2 Å) distances. The assignment of the oxidation states is evident from the bond valence sum calculations on the Mo centers (Table S3) as well as the results of XPS analysis (Figure S7). This represents the initial preparation of the Zn-ε-Keggin-Cl fragment. It is of great importance to isolate this Zn-ε-Keggin-based monomer. As suggested by DFT calculations, this monomer may serve as an intermediate during the formation of POM-based MOFs. With the guidance of DFT calculations, we

DOI: 10.1021/jacs.5b02688
J. Am. Chem. Soc. 2015, 137, 7169−7177

successfully synthesized **NENU-500** and **NENU-501** by the coordination of Zn-ε-Keggin units with organic linkers.

NENU-500. Single-crystal X-ray diffraction analysis reveals that **NENU-500** crystallizes in the space group of $Ia\bar{3}d$ (No. 230). The asymmetric unit contains one $[\varepsilon\text{-}PMo^{V}_{8}Mo^{VI}_{4}O_{36}(OH)_{4}Zn_{4}]^{+}$ ion (Figure S8), a BTB^{3-} fragment with 4/3 of occupancy, three TBA^{+} cations, and guest molecules. Electrons of the ε-Keggin unit in **NENU-500** are highly delocalized owing to the high symmetry, as confirmed by the bond valence sum calculations (Table S3). **NENU-500** is dark red (Figure S9), which is the typical color of reduced molybdenum blue species[18] and is in agreement with the XPS analysis (Figure S10). Each Zn-ε-Keggin fragment is coordinated by four BTB^{3-} linkers, and each BTB^{3-} connects three Zn-ε-Keggin units (Figure S11). Such connectivity leads to a 3D porous extended framework with a typical **ctn** topology (Figure 1b).[19] Only a few frameworks with **ctn** topology have been documented;[20] however, POM-based MOFs with **ctn** topology are rarely reported. As postulated by Aristotle, "Nature abhors a vacuum." In order to minimize the void cavities and stabilize the framework, the single network allows another identical network to penetrate, thus resulting in a two-fold interpenetrated **ctn** array (Figure 1c).[21] In Dolbecq's original work,[13a] 1,3,5-benzenetricarboxylic acid (H_3BTC) was employed as a linker to connect with a tetrahedral Zn-ε-Keggin moiety, resulting in a POM-based framework with **ofp** topology (designated as $\boldsymbol{\varepsilon(trim)_{4/3}}$). It is interesting to note that, in the two compounds, though BTB^{3-} and BTC^{3-} are both tritopic linkers and the Zn-ε-Keggin unit acts as a tetrahedral node, the final products hold two distinct types of topology, which perhaps can be attributed to the different types of point group symmetry of the 3-connected nodes.[20b] It could also be due to the interpenetration in **NENU-500**, made possible by the elongated linkers, which could stabilize its **ctn** net.[20b] X-ray diffraction analysis indicates that a 1D channel can be observed running parallel to the [111] direction in **NENU-500**, and enclosed in the channel are disordered bulky TBA^{+} counter-cations and guest molecules. However, the positions of TBA^{+} ions and guest molecules could not be determined by X-ray diffraction study due to severe crystallographic disorder. The TBA^{+} ions serve for structure directing agents, space filling, and charge balance.

NENU-501. The substitution of H_3BTB by H_3BPT under similar conditions yielded **NENU-501** (Figure S12). **NENU-501** crystallizes in the monoclinic space group $C2/c$ (No. 15). The asymmetric unit comprises one neutral $\{\varepsilon\text{-}PMo^{V}_{8}Mo^{VI}_{4}O_{37}(OH)_{3}Zn_{4}\}$ fragment (Figure S13), one BPT^{3-} moiety, and three TBA^{+} ions. In **NENU-501**, the building block is not the expected Zn-ε-Keggin but a dimerized form of Zn-ε-Keggin as reported in the literature (Figure 2).[13a] The dimeric Zn-ε-Keggin unit perhaps results from the aggregation of two monomeric Zn-ε-Keggin units. The dimeric Zn-ε-Keggin fragment has six anchoring points, exhibiting the staggered conformation of ethane. Each BPT^{3-} unit bridges three dimeric fragments to give rise to a 3D (3,6)-connected network with flu-3,6-$C2/c$ topology (Figures 2 and S14).[22] Due to the dimerization, the ratio of Zn-ε-Keggin to organic linker is 1 instead of 4/3 as in **NENU-500**. As in **NENU-500**, the charge of the anionic framework is balanced by TBA^{+} cations located in the channels of **NENU-501**.

The phase purities of **NENU-499**–**NENU-501** were established by comparison of their observed and simulated powder X-ray diffraction (PXRD) patterns (Figures S15 and S16). **NENU-500** and **NENU-501** show good thermal stabilities in air, with decomposition starting at 300 and 366 °C, respectively. **NENU-500** exhibits a continuous weight loss step from 300 to 560 °C, corresponding to the loss of all organic ligands, guest molecules, and TBA^{+} ions. **NENU-501** exhibits a continuous weight loss step from 366 to 554 °C, corresponding to the loss of all organic ligands and TBA^{+} ions. The residue corresponds to ZnO and MoO_3. Furthermore, **NENU-500** and **NENU-501** are air-stable, maintaining their crystallinities for at least several months, and no efflorescence was observed. As polymeric materials, they are insoluble in common organic solvents, such as dimethyl sulfoxide (DMSO), chloroform, ethanol, and acetone. Remarkably, these POM-based MOFs are also stable in acidic and basic aqueous solutions in the pH range of 1–12 at room temperature, as confirmed by the subsequent PXRD and FT/IR measurements (Figures 3, S17, and S18). MOFs stable in both acidic and basic solutions are rare,[23] especially for POM-based compounds, which often disintegrate in basic solutions. However, stability over a wide range of pH values is a prerequisite for HER catalysts of this kind.

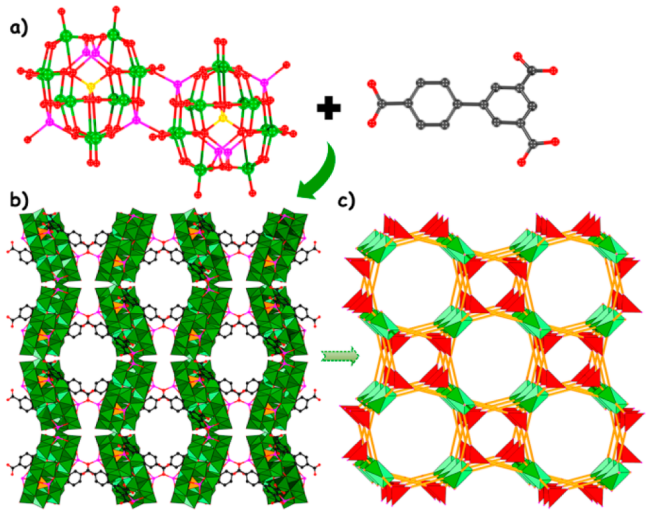

Figure 2. Summary of the structure of **NENU-501**: (a) dimeric Zn-ε-Keggin unit and BPT^{3-} fragment as building blocks, (b) 3D framework, and (c) (3,6)-connected topology.

After activation of the as-synthesized materials by immersing a sample in methanol for 3 days and then heating at 100 °C under a vacuum overnight, **NENU-500** retained its crystallinity, as confirmed by PXRD studies (Figure S19). The N_2 adsorption isotherms at 77 K of the activated sample **NENU-500a** revealed a typical type I isotherm characteristic for a microporous material with a slight hysteresis between adsorption and desorption (Figure S20), which can be explained by the dynamic feature of the framework.[24] The maximum N_2 adsorption amount was 100.0 $cm^3 \cdot g^{-1}$ at standard temperature and pressure (STP). The Brunauer–Emmett–Teller (BET) surface area was calculated to be 195 $m^2 \cdot g^{-1}$ based on the N_2 adsorption data. The BET surface area was not very high, which perhaps can be assigned to partial exchange of TBA^{+} ions. However, it is still higher than other metal-based nanomaterials as electrocatalysts,[25] and should provide adequate opportunity for electricity, water, and solvent to move through inner pore spaces, unlike nonporous HER catalysts, which will only be catalytically active along their surfaces. The architectural stability and permanent porosity of

DOI: 10.1021/jacs.5b02688
J. Am. Chem. Soc. 2015, 137, 7169–7177

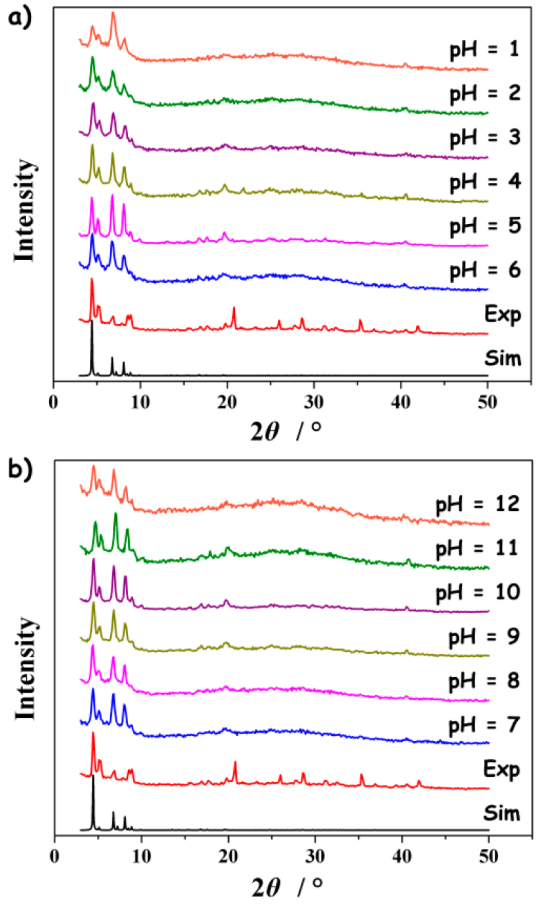

Figure 3. PXRD patterns of **NENU-500**, with the as-synthesized sample immersed in water with different pH values at room temperature for 24 h. "Sim" represents the simulated pattern, and "Exp" represents the pattern of as-synthesized sample.

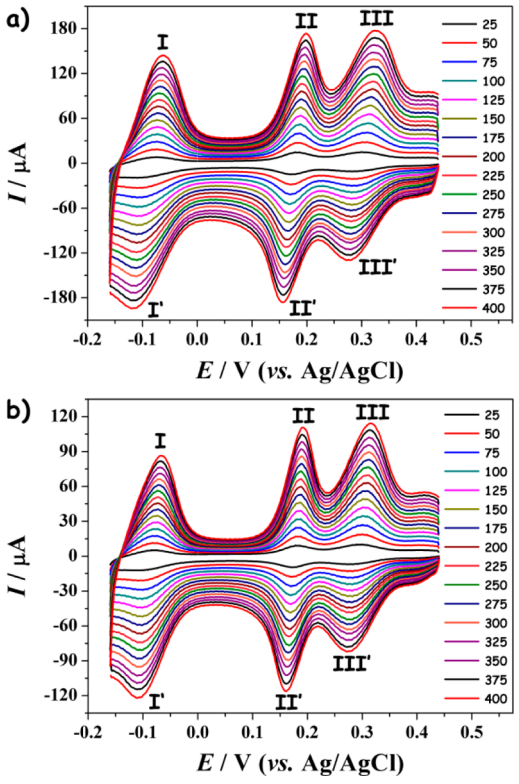

Figure 4. CVs of **NENU-500**-GCE (a) and **NENU-501**-GCE (b) at different scan rates ($mV \cdot s^{-1}$), both measured in 0.1 $mol \cdot L^{-1}$ H_2SO_4 aqueous solution.

NENU-500 were confirmed by the N_2 adsorption experiments. **NENU-501** was treated under similar conditions; however, little N_2 adsorption was detected. This perhaps can be attributed to the very small pore of **NENU-501**, in which the TBA^+ ions were not removable. To obtain more knowledge of the adsorption properties, water adsorption isotherms of **NENU-500** were measured at 293 K. As shown in Figure S21, the water uptake increases as P/P_0 increases and reaches 66.9 $cm^3 \cdot g^{-1}$ (2.99 $mol \cdot kg^{-1}$) at P/P_0 = 0.99.

Owing to their strong tolerance to both acidic and basic media and ideal electrical conductivity, carbon materials with various structures are widely used as skeletons to support host materials, resulting in advanced materials for electrocatalysis and other energy-related applications.[26] Therefore, we prepare the composite catalysts based on the powder samples of the as-synthesized materials and carbon black (Vulcan XC-72R). The electrochemical behaviors of **NENU-499**−**NENU-501**-carbon black (Vulcan XC-72R) on glassy carbon electrode (GCE) were studied;[27] in particular, studies of the electrocatalytic activities of **NENU-500** and **NENU-501** toward NO_2^- ions were carried out. **NENU-499** exhibits three redox peaks in 0.1 $mol \cdot L^{-1}$ H_2SO_4 aqueous solution, and the approximate proportionality of the peak II−II′ currents to the scan rates from 25 to 200 $mV \cdot s^{-1}$ suggests that the redox process is surface-controlled for **NENU-499**-GCE (Figure S22). Figure 4 displays typical cyclic voltammograms (CVs) at potentials ranging from −0.16 to +0.45 V (vs Ag/AgCl) in 0.1 $mol \cdot L^{-1}$ H_2SO_4 aqueous solution at different scan rates for **NENU-500** and **NENU-501**-GCE. The mean peak potentials $E_{1/2} = (E_{pa} + E_{pc})/2$ for **NENU-500** appeared at about −0.091 (I−I′), +0.176 (II−II′), and +0.296 V (III−III′) with peak potential separations of 35, 13, and 23 mV (scan rate: 50 $mV \cdot s^{-1}$), respectively. The mean peak potentials for **NENU-501** appeared at about −0.092 (I−I′), +0.177 (II−II′), and +0.288 V (III−III′) with peak potential separations of 26, 12, and 22 mV (scan rate: 50 $mV \cdot s^{-1}$), respectively. These data are consistent with those reported in the literature.[28] The approximate proportionality of the three redox peak currents to the scan rates from 25 to 400 $mV \cdot s^{-1}$ indicates that the redox process is surface-controlled for **NENU-500** and **NENU-501**-GCE (Figures S23 and S24).[29] In addition, **NENU-500** and **NENU-501**-GCE are highly stable, and the peak potentials change little with the increasing scan rates, which is especially useful for electrocatalytic studies. **NENU-500** and **NENU-501**-GCE display good electrocatalytic activities in a wide concentration range toward the reduction of NO_2^- ions (Figures S25 and S26). Upon the addition of $NaNO_2$, the reduction peak currents dramatically increase, and the corresponding oxidation peak currents decrease, illustrating that nitrite ion is reduced.[30]

Furthermore, the HER catalytic activities of as-synthesized **NENU-499**−**NENU-501** were also evaluated by electrochemical experiments. These experiments were carried out in 0.5 M H_2SO_4 aqueous solution (pH = 0.16).[31] Figure S27 shows the polarization curve of an **NENU-500**-modified electrode in 0.5 M H_2SO_4 with a scan rate of 5 $mV \cdot s^{-1}$. In order to clarify the factors contributing to the HER performance of the **NENU-500** rotating disk electrode (RDE), the HER activity of pure XC-72R-modified electrode

DOI: 10.1021/jacs.5b02688
J. Am. Chem. Soc. 2015, 137, 7169−7177

was measured as the reference. As a comparison, **NENU-500**-doped composites with different contents were also studied. The onset potential for HER of **NENU-500**-doped XC-72R composites modified electrodes is more positive than that of XC-72R-modified electrode. Meanwhile, the current density of **NENU-500**-doped XC-72R composites modified electrodes is also larger than those of pure **NENU-500** or XC-72R electrode when the potential is more negative than 140 mV. That is, the HER activity of **NENU-500**-modified electrode is evidently enhanced after carbon black doping. These results demonstrate that the HER activity of POM-based MOF-modified electrodes mainly originates from the synergistic effect between the POM-based MOF material and carbon black. After careful analysis of these results, we infer that **NENU-500** may contribute to the low overpotential, and carbon black contributes to the high current density. It is necessary to dope carbon black into POM-based MOF, which not only improves the electrical conductivity but also increases the current. The increased content of **NENU-500** in composite electrode facilitates charge transfer to some extent and thereby results in improved HER activity. For instance, the composite with 50 wt % MOF exhibits better catalytic behavior than composite with 20 wt % MOF. **NENU-500** (50 wt %) shows an onset overpotential of 180 mV and a Tafel slope of 96 mV·dec^{-1}.

Additionally, a series of control experiments were also performed under the given conditions. Figure 5a shows the HER polarization curves of various electrocatalysts in 0.5 M H_2SO_4 aqueous solution with a scan rate of 5 mV·s^{-1}, including those of **NENU-499**-, **NENU-500**-, and **NENU-501**-modified RDE with loading amount of 50 wt % as well as bare RDE, pure XC-72R, and commercial Pt/C (20 wt % Pt/XC-72R). Moreover, the HER activities of $\boldsymbol{\varepsilon}(\mathbf{trim})_{4/3}$, **NENU-5**, and **HKUST-1** were also studied for comparison (Figure S28). As expected, among all tested electrodes, Pt/C exhibits the highest activity for HER with nearly zero onset overpotential (η) and a high current density. Bare RDE shows the lowest HER activity among all tested electrodes. Pure XC-72R has negligible electrocatalytic activity, while the doped samples could enhance the HER activity by the introduction of active sites. **NENU-500**-modified RDE is highly active toward HER, and it can approach a large current density of 10 mA·cm^{-2} at an overpotential of 237 mV. To compare the required overpotentials for driving a current of 10 mA·cm^{-2} (η_{10}) is more practical owing to the fact that a solar light-coupled HER apparatus usually runs at 10−20 mA·cm^{-2} under the standard conditions (1 sun, AM 1.5),[2] indicating that 10 mA·cm^{-2} is meaningful as the point of reference. **NENU-501** and $\boldsymbol{\varepsilon}(\mathbf{trim})_{4/3}$ require an overpotential of 392 and 515 mV to achieve a 10 mA·cm^{-2} HER current density, respectively. In addition, **NENU-499**-modified RDE requires an overpotential of 570 mV, which is larger than those of **NENU-500**, **NENU-501**, and $\boldsymbol{\varepsilon}(\mathbf{trim})_{4/3}$. The η_{10} values were determined to be 585 and 691 mV for **NENU-5**- and **HKUST-1**-modified electrodes (Table 1), respectively, which are even larger than those of the other four electrocatalysts. Among the six tested, five MOF composite electrodes exhibit larger overpotentials than that of **NENU-500** composite electrode, suggesting that fast and efficient electron transfer occurs on the **NENU-500** modified electrode. The results imply that **NENU-500** is superior in catalytic activity over the other five electrocatalysts, suggesting that both POM units and porosity are essential for high electrocatalytic activity.

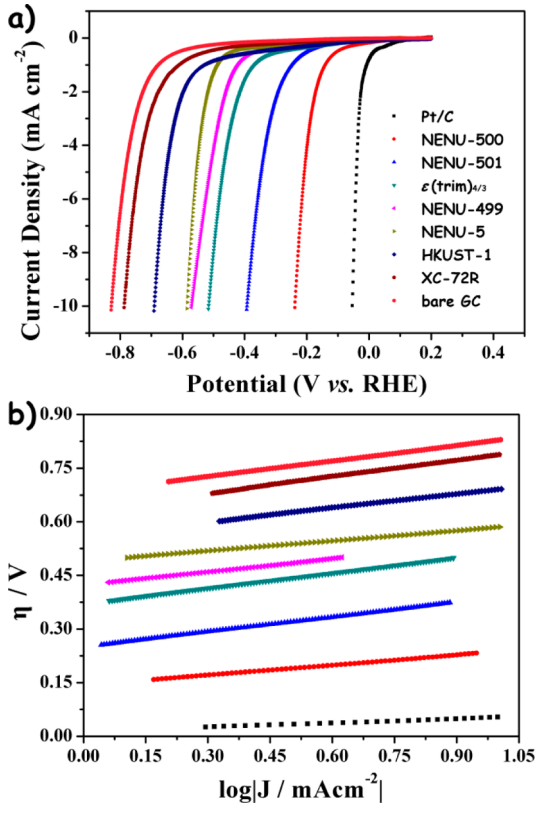

Figure 5. Electrochemical characterization of the prepared catalysts: (a) polarization curves in 0.5 M H_2SO_4 aqueous solution and (b) the corresponding Tafel plots.

Tafel slope is an inherent property of electrocatalytic material, which is determined by the rate-limiting step of HER. Additionally, the determination and interpretation of Tafel slope are of importance for the elucidation of HER mechanism involved. Figure 5b displays the Tafel plots for **NENU-499**−**NENU-501**. Meanwhile, the Tafel plots for $\boldsymbol{\varepsilon}(\mathbf{trim})_{4/3}$, **NENU-5**, **HKUST-1**, XC-72R, and Pt/C are also presented for comparison. The linear portions of the Tafel plots are fitted to the Tafel equation ($\eta = b \log|j| + a$, where j is the current density, b is the Tafel slope, and a is the intercept relative to the exchange current density j_0). Commercial Pt/C shows the Tafel slope of ∼30 mV·dec^{-1} that is in agreement with the reported value,[32] confirming the validity of our electrochemical measurements. The Tafel slopes of **NENU-500**, **NENU-501**, $\boldsymbol{\varepsilon}(\mathbf{trim})_{4/3}$, **NENU-499**, **NENU-5**, and **HKUST-1** obtained from the Tafel plots are 96, 137, 142, 122, 94, and 127 mV·dec^{-1}, respectively. The exchange current density (j_0) of **NENU-500** is calculated to be about 0.036 mA·cm^{-2}. Compared with those non-noble-metal electrocatalytic materials reported recently, **NENU-500** electrode presents a quite large exchange current density and a relatively small Tafel slope,[33] suggesting **NENU-500** is a promising low-cost and earth-abundant metallic electrocatalyst for HER.

A promising material for electrocatalytic HER should exhibit not only high activity but also good durability. Therefore, we also examined the stability of **NENU-500** and **NENU-501** in hydrogen generation by accelerated degradation experiment. As shown in Figure S29, after continuous CV scanning for 2000 cycles in 0.5 M H_2SO_4 aqueous solution at a scan rate of 100 mV·s^{-1}, the polarization curves show negligible difference compared with the initial one. The result demonstrates that

DOI: 10.1021/jacs.5b02688
J. Am. Chem. Soc. 2015, 137, 7169−7177

Table 1. Comparison of HER Activity Data for Different Catalysts

catalyst	onset potential (mV)	η_{10} (mV)	Tafel slope (mV·dec^{-1})	j_0 (A·cm^{-2})	R^{2a}	$R_{ct}{}^b$ (Ω)
Pt/C	25	52	30	3.4×10^{-4}	0.99617	—[c]
NENU-500	180	237	96	3.6×10^{-5}	0.99982	28
NENU-501	304	392	137	1.5×10^{-5}	0.99982	58
$\boldsymbol{\varepsilon}$**(trim)**$_{4/3}$	420	515	142	2.4×10^{-6}	0.99989	3309
NENU-499	452	570	122	3.4×10^{-7}	0.99957	—[c]
NENU-5	518	585	94	6.1×10^{-9}	0.99986	2381
HKUST-1	612	691	127	3.6×10^{-8}	0.99966	1253
XC-72R	677	787	154	7.8×10^{-8}	0.99928	—[c]
bare GC	709	829	144	1.8×10^{-8}	0.99989	—[c]

[a]Adjusted R^2 of Tafel plots. [b]Extracted from fitting electrochemical impedance spectra measured at −550 mV (vs Ag/AgCl) to an equivalent circuit. [c]Not measured.

NENU-500 and **NENU-501** modified electrodes are durable during electrocatalytic hydrogen production. Furthermore, their stabilities in 0.5 M H_2SO_4 aqueous solution were also evaluated by immersing as-synthesized **NENU-500** and **NENU-501** in acidic solution for 6 h. From the PXRD patterns, it can be clearly seen that the peaks keep the positions (Figure S16), suggesting the maintenance of the frameworks. In addition, the PXRD patterns of **NENU-5**, and **HKUST-1** treated under the same conditions cannot keep the peak positions (Figure S30), indicating they are not stable in 0.5 M H_2SO_4 aqueous solution. Especially, the color and appearance of **HKUST-1** immediately changed once soaked in 0.5 M H_2SO_4 aqueous solution. The results reveal that **NENU-500** and **NENU-501** have superior stability in a long-term electrochemical process compared to **NENU-5**, and **HKUST-1**.

To get further insight into the activity of as-synthesized **NENU-500** and **NENU-501** modified electrodes toward HER, electrochemical impedance spectroscopy (EIS) analysis was also performed. Figures 6a and S31 describe the obtained Nyquist plots of **NENU-500** and **NENU-501**, and the magnified Nyquist plots in high-frequency region are presented for clarity (upper inset). The data were fitted to an equivalent circuit (Figures S31), and the resultant fitting parameters are summarized in Table S4. The charge-transfer resistance (R_{ct}) at the surface of the catalysts is determined from the diameter of a semicircle at high frequencies in the Nyquist plot. Generally, R_{ct} value varies inversely with the electrocatalytic activity. That is, smaller diameter corresponds to faster HER kinetics. The R_{ct} values of **NENU-500** (28 Ω) and **NENU-501** (58 Ω) measured at −550 mV (vs Ag/AgCl) are much lower than those of $\boldsymbol{\varepsilon}$**(trim)**$_{4/3}$ (3309 Ω), **NENU-5** (2381 Ω), and **HKUST-1** (1253 Ω) (Figure 6b). Thus, such a low R_{ct} value of **NENU-500** indicates that its high electrocatalytic activity for HER could be ascribed to the highly conductive carbon black hybrid improving the charge transfer characteristics of **NENU-500**.

As suggested by Nørskov et al.,[34] a good hydrogen evolution catalyst should have a free energy of adsorbed H close to that of the reactant or product (i. e., $\Delta G^0_H \approx 0$), which can provide a fast proton/electron-transfer step as well as a fast hydrogen release processes. To get a deeper understanding, we select Zn-ε-Keggin-Cl fragment as a model to compute the free energy change for H adsorption by means of DFT computations, owing to the presence of Zn-ε-Keggin unit in both **NENU-500** and **NENU-501**. As shown in Figure S32, there are three possible H adsorption sites on Zn-ε-Keggin-Cl, namely μ_3-bridging oxygen (O_a), μ_2-bridging oxygen (O_b), and terminal oxygen (O_t). According to our computations, O_a site is more favorable for H adsorption with its adsorption energy (−0.56 eV) lower than those of O_b site (0.22 eV) and O_t site (0.52 eV), respectively. By taking entropy and zero point energy into account, the free energy change for H adsorption on O_a site is computed to be −0.07 eV, indicating that Zn-ε-Keggin-Cl truly has a good catalytic capacity for hydrogen evolution. This is one of the reasons that **NENU-500** and **NENU-501** possess higher activity than other MOF materials.

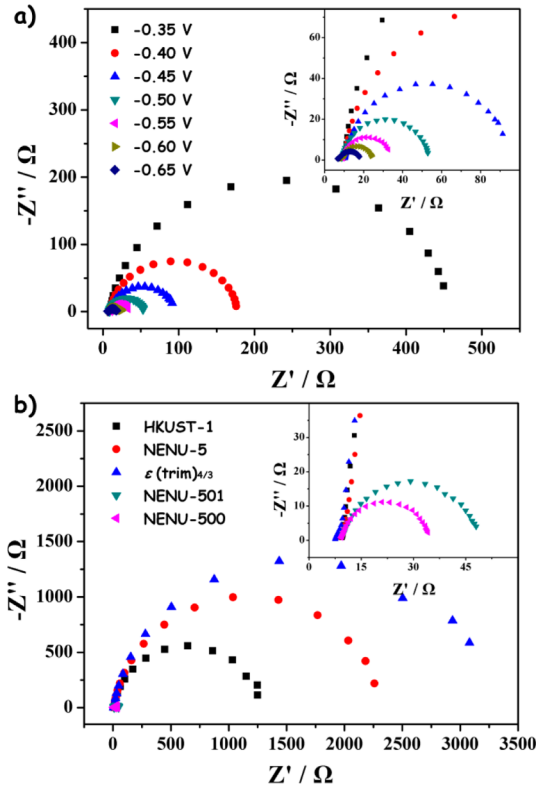

Figure 6. Nyquist plots of (a) **NENU-500** examined at different potentials and (b) the different as-synthesized catalysts examined at −0.55 V (vs Ag/AgCl). Inset denotes the magnified images of high-frequency region.

NENU-500 exhibits the highest HER activity among **NENU-501**, $\boldsymbol{\varepsilon}$**(trim)**$_{4/3}$, **NENU-499**, **NENU-5**, and **HKUST-1**, which perhaps can be assigned to the following reasons: (i) The poor HER activity of **HKUST-1**, below those of the other five polymolybdate-based catalysts, can be assigned to the fact that it does not contain active sites of molybdophosphate fragment and its poor stability in 0.5 M H_2SO_4 aqueous solution. (ii) The lower HER activity of **NENU-5** compared to those of **NENU-**

DOI: 10.1021/jacs.5b02688
J. Am. Chem. Soc. 2015, 137, 7169−7177

500, **NENU-501**, and $\boldsymbol{\varepsilon(trim)_{4/3}}$ perhaps can be attributed to the structure factor.[12] In **NENU-5**, the α-$PMo_{12}O_{40}$ unit works as a template located in the channel, while in **NENU-500**, **NENU-501**, and $\boldsymbol{\varepsilon(trim)_{4/3}}$, the ε-Keggin moiety serves as a node to directly connect with organic ligands, leading to more accessible active sites. In addition, **NENU-5** was also unstable in 0.5 M H_2SO_4 aqueous solution. (iii) The higher HER activity of **NENU-499** compared to those of the non-POM-containing materials suggests that Zn-ε-Keggin fragment can lower the overpotential. Furthermore, the rigid and stable frameworks of **NENU-500**, **NENU-501**, and $\boldsymbol{\varepsilon(trim)_{4/3}}$ allow for easy diffusion of electrolyte, leading to more efficient utilization of active sites than in **NENU-499**. (iv) The higher HER activity of **NENU-500** compared to those of **NENU-501** and $\boldsymbol{\varepsilon(trim)_{4/3}}$ can be attributed to the porosity factor. **NENU-501** and $\boldsymbol{\varepsilon(trim)_{4/3}}$ are essentially nonporous, as revealed by nitrogen adsorption studies, most likely due to an inability to remove a large TBA^+ cation from their small pores. **NENU-500**, on the other hand, exhibits permanent porosity. Furthermore, **NENU-500** has a much lower R_{ct} than those of **NENU-501** and $\boldsymbol{\varepsilon(trim)_{4/3}}$, which results in much faster electrode kinetics.[35] As a result, the stable porous POM-based MOF with POM node directly connecting with organic linker exhibits the highest HER activity as an electrocatalyst, which will be a new promising branch of POM-based MOF materials as HER catalysts. In other words, POM structural nodes and permanent porosity are two prerequisites for POM-based electrocatalysts.

CONCLUSIONS

In conclusion, two POM-based materials, **NENU-500** and **NENU-501**, were successfully isolated, which comprise POM structural nodes and organic linkers. In addition, **NENU-500** represents a rare example of 3D porous POM-based MOF with a **ctn** net topology. **NENU-500** and **NENU-501** exhibit not only good air stability but also acid and base tolerance. Therefore, **NENU-500** and **NENU-501**, as POM-based materials, were utilized as electrocatalysts toward HER, owing to the combination of the redox property of POM moieties and the porosity of MOFs. Remarkably, **NENU-500** is highly active for electrochemically generating hydrogen from water under acidic conditions, with a Tafel slope of 96 $mV{\cdot}dec^{-1}$ and an exchange current density of 0.036 $mA{\cdot}cm^{-2}$. It should be noted that **NENU-500** exhibits the best HER performance among all MOF materials due to its good stability, porosity, and exposed active sites. Furthermore, the HER activities of **NENU-500** and **NENU-501** were maintained after 2000 cycles. The facile preparation of these POM-based materials, along with their long-term aqueous stability, low overpotential, and high activity, offers promising features for their potential use in hydrogen generation. The present study not only demonstrates a successful case to construct stable POM-based MOFs with porosity but also provides novel hydrogen-evolving electrocatalysts with excellent activity. We are convinced that this newly emerging hydrogen-evolving electrocatalyst is bubbling with opportunities and that significant progress will be made in the years ahead. More investigation is currently underway in our group.

EXPERIMENTAL SECTION

Materials. All the chemicals were obtained from commercial sources and were used without further purification. Deionized water was used for preparation of **NENU-499**–**NENU-501**, and ultrapure water (resistivity: $\rho \geq 18$ $M\Omega{\cdot}cm^{-1}$) was used in electrochemical experiments. IR spectra were collected in the range 4000–400 cm^{-1} using KBr pellets on an Alpha Centaurt FT/IR spectrophotometer. PXRD measurements were recorded ranging from 3 to 50° at room temperature on a Bruker D8 Advance diffractometer with Cu K_α (λ = 1.5418 Å). Thermogravimetric analysis (TGA) of the samples was performed using a PerkinElmer TG-7 analyzer heated from room temperature to 700 °C under nitrogen at the heating rate of 5 $°C{\cdot}min^{-1}$. XPS analysis was performed on a thermo ECSALAB 250 spectrometer with an Al Kα (1486.6 eV) achromatic X-ray source running at 15 kV. The XPS binding energy (BE) was internally referenced to the aliphatic C(1s) peak (BE, 284.6 eV). Field-emission scanning electron microscopy (FE SEM) images were obtained with a Hitachi SU-8010 electron microscope (Hitachi, Tokyo, Japan).

Preparation of NENU-499. A mixture of sodium molybdate dihydrate (618 mg, 2.55 mmol), Mo powder 99.99% (50 mg, 0.52 mmol), H_3PO_3 (20 mg, 0.25 mmol), zinc chloride (136 mg, 1.00 mmol), tetrabutylammonium hydroxide 40 wt % solution in water (120 μL, 0.18 mmol), and H_2O (8 mL) was stirred for 20 min, and the pH was acidified to 4.8 with diluted HCl (2 M). Then, 6-nitrobenzimidazole (82 g, 0.50 mmol) was added to the mixture, which was transferred and sealed in a 15 mL Teflon-lined stainless steel container and heated at 180 °C for 72 h. After cooling to room temperature at 10 $°C{\cdot}h^{-1}$, dark-red crystals suitable for XRD study were harvested.

Preparation of NENU-500 and NENU-501. A mixture of $Na_2MoO_4{\cdot}2H_2O$ (618 mg, 2.55 mmol), Mo powder 99.99% (50 mg, 0.52 mmol), H_3PO_3 (20 mg, 0.25 mmol), zinc chloride (136 mg, 1.00 mmol), H_3BTB (130 mg, 0.30 mmol), tetrabutylammonium hydroxide 40 wt % solution in water (120 μL, 0.18 mmol), and H_2O (7 mL) was stirred for 20 min, and the pH was acidified to 4.8 with diluted HCl (2 M). Then, the mixture was transferred and sealed in a 15 mL Teflon-lined stainless steel container and heated at 180 °C for 72 h. After cooling to room temperature at 10 $°C{\cdot}h^{-1}$, dark-red crystals (**NENU-500**) suitable for XRD study were harvested (yield 68% based on H_3BTB). IR (Figure S3, KBr pellets, ν/cm^{-1}): 3450 (s), 2961 (m), 1599 (m), 1550 (w), 1466 (w), 1376 (m), 1110 (w), 935 (m), 814 (m), 780 (m), 705 (m), 587 (m). **NENU-501** was isolated by an analogous method with **NENU-500**, only using H_3BPT in substitution for H_3BTB. IR (Figure S3, KBr pellets, ν/cm^{-1}): 3445 (w), 2961 (m), 2872 (m), 1559 (m), 1470 (m), 1350 (s), 1148 (w), 942 (s), 819 (s), 777 (s), 707 (m), 590 (m), 486 (w).

Single-Crystal X-ray Crystallography. Suitable single crystals were selected and mounted onto the end of a thin glass fiber using Fomblin oil. Single-crystal XRD data were recorded on a Bruker APEXII CCD diffractometer with graphite-monochromated Mo Kα radiation (λ = 0.71073 Å) at 293 K. Absorption corrections were applied using multiscan technique. The structure was solved by Direct Method of SHELXS-97[36a] and refined by full-matrix least-squares techniques using the SHELXL-97 program[36b] within WINGX.[36c] For **NENU-500**, the TBA^+ cations could not be located in the structure due to severe crystallographic disorder, and the data were corrected with SQUEEZE,[37] a part of the PLATON package of crystallographic software used to calculate the solvent molecules or counterions disorder area and to remove the contribution to the overall intensity data. The crystallographic information is presented in Table S2.

Electrochemical Measurements. Cyclic voltammetry (CV) and linear sweep voltammetry (LSV) tests were conducted with a CHI830B workstation (CH Instruments, China) in a conventional three electrode system. A modified GCE (d = 3 or 5 mm) served as the working electrode in electrochemical experiments, a platinum wire as the counter electrode, and an Ag/AgCl electrode as the reference electrode, respectively. In addition, the GCE with diameter of 5 mm was used as rotating disk electrode (RDE, 0.19625 cm^2, Princeton Applied Research Instrumentation, USA). Meanwhile, a speed control unit-Princeton Applied Research Model 616 Electrode Rotator was used for RDE measurements. In the identical cell setup, EIS was carried out on a PARSTAT 2273 electrochemical system (Princeton Applied Research Instrumentation, USA). The frequency range covers from 10.0 kHz to 0.1 Hz with modulation amplitude of 10 mV at different bias voltages. Prior to measurement, the solution was bubbled

DOI: 10.1021/jacs.5b02688
J. Am. Chem. Soc. 2015, 137, 7169–7177

with nitrogen gas for 30 min to remove dissolved oxygen. In the measurements, the Ag/AgCl reference electrode was calculated with respect to RHE according to reported method.[38] The formula is $E(\mathrm{RHE}) = E(\mathrm{Ag/AgCl}) + 0.059\ \mathrm{pH} + 0.198$ V, where E(RHE) is a potential vs RHE, E(Ag/AgCl) is a potential vs Ag/AgCl electrode, and pH is the pH value of electrolyte. LSV measurements were carried out in 0.5 M H_2SO_4 with a scan rate of 5 $mV{\cdot}s^{-1}$, which were examined after 500 cycles of CV tests in the range of 0 to −1.2 V to stabilize the current. The working electrode was rotated at 1000 rpm to remove hydrogen gas bubbles formed at the catalyst surface. The durability tests were carried out by repeating the potential scan from 0 to −1 V at a scan rate of 100 $mV{\cdot}s^{-1}$ for 2000 cycles. All current densities are the ratios of currents and geometric areas of working electrodes. The EIS spectra were fitted by the Z-SimpWin software.

Preparation of Working Electrodes. A mixture of 20 mg of carbon black (Vulcan XC-72R) and the desired amount of as-synthesized POM-based MOFs (20 or 5 mg) was co-grounded for 45 min. Prior to be modified, the GCE and RDE were polished carefully with 0.05 μm alumina powders and then cleaned with HNO_3 (1:1), ethanol, and deionized water, respectively. Catalyst ink was prepared by mixing 5 mg of the prepared catalyst powders into water (950 μL) containing 0.5 wt % Nafion (50 μL) and then ultrasonically dispersed for 30 min. Then an aqueous dispersion was transferred onto the clean-washed GCE (5 μL) and RDE (14.2 μL) and dried in air at room temperature before electrochemical experiments.

■ ASSOCIATED CONTENT

Ⓢ Supporting Information

Computational details, figures, tables and crystallographic data in CIF format. The Supporting Information is available free of charge on the ACS Publications website at DOI: 10.1021/jacs.5b02688.

■ AUTHOR INFORMATION

Corresponding Authors

*zmsu@nenu.edu.cn
*yqlan@njnu.edu.cn
*zhou@chem.tamu.edu

Notes

The authors declare no competing financial interest.

■ ACKNOWLEDGMENTS

The synthetic and structural studies of this research was supported by the Center for Gas Separations Relevant to Clean Energy Technologies, an Energy Frontier Research Center funded by the U.S. Department of Energy, Office of Science, Office of Basic Energy Sciences under Award Number DE-SC0001015. It was financially partially supported by Pre-973 Program (2010CB635114), the National Natural Science Foundation of China (nos. 21371099, 21401021 and 21403033), China Postdoctoral Science Foundation (no. 2014M551154), the Science and Technology Development Planning of Jilin Province (nos. 20140520089JH and 20140203006GX), the Jiangsu Specially-Appointed Professor, the NSF of Jiangsu Province of China (no. BK20130043), the Priority Academic Program Development of Jiangsu Higher Education Institutions, the Foundation of Jiangsu Collaborative Innovation Center of Biomedical Functional Materials, and the Fundamental Research Funds for the Central Universities (no. 14QNJJ013). We thank Prof. Da-Qiang Yuan (Fujian Institute of Research on Structure of Matter, Chinese Academy of Sciences) for structure refinement in crystallography. We thank Mr. Mathieu Bosch and Dr. Qiang Zhang for their helpful language editing throughout the manuscript.

■ REFERENCES

(1) (a) Dresselhaus, M. S.; Thomas, I. L. *Nature* **2001**, *414*, 332−337. (b) Turner, J. A. *Science* **2004**, *305*, 972−974.

(2) Walter, M. G.; Warren, E. L.; McKone, J. R.; Boettcher, S. W.; Mi, Q.; Santori, E. A.; Lewis, N. S. *Chem. Rev.* **2010**, *110*, 6446−6473.

(3) (a) Merki, D.; Hu, X. *Energy Environ. Sci.* **2011**, *4*, 3878−3888. (b) Boettcher, S. W.; Warren, E. L.; Putnam, M. C.; Santori, E. A.; Turner-Evans, D.; Kelzenberg, M. D.; Walter, M. G.; McKone, J. R.; Brunschwig, B. S.; Atwater, H. A.; Lewis, N. S. *J. Am. Chem. Soc.* **2011**, *133*, 1216−1219.

(4) (a) Hambourger, M.; Gervaldo, M.; Svedruzic, D.; King, P. W.; Gust, D.; Ghirardi, M.; Moore, A. L.; Moore, T. A. *J. Am. Chem. Soc.* **2008**, *130*, 2015−2022. (b) Le, G. A.; Artero, V.; Jousselme, B.; Tran, P. D.; Guillet, N.; Métayé, R.; Fihri, A.; Palacin, S.; Fontecave, M. *Science* **2009**, *326*, 1384−1387.

(5) (a) Chen, W.-F.; Sasaki, K.; Ma, C.; Frenkel, A. I.; Marinkovic, N.; Muckerman, J. T.; Zhu, Y.; Adzic, R. R. *Angew. Chem., Int. Ed.* **2012**, *51*, 6131−6135. (b) Liu, Y.; Yu, H.; Quan, X.; Chen, S.; Zhao, H.; Zhang, Y. *Sci. Rep.* **2014**, *4*, 6843. (c) Xiao, P.; Sk, M. A.; Thia, L.; Ge, X.; Lim, R. J.; Wang, J.-Y.; Lim, K. H.; Wang, X. *Energy Environ. Sci.* **2014**, *7*, 2624−2629. (d) Tian, J.; Liu, Q.; Asiri, A. M.; Sun, X. *J. Am. Chem. Soc.* **2014**, *136*, 7587−7590. (e) Jiang, P.; Liu, Q.; Liang, Y.; Tian, J.; Asiri, A. M.; Sun, X. *Angew. Chem., Int. Ed.* **2014**, *53*, 12855−12859. (f) Liu, Q.; Tian, J.; Cui, W.; Jiang, P.; Cheng, N.; Asiri, A. M.; Sun, X. *Angew. Chem., Int. Ed.* **2014**, *53*, 6710−6714. (g) Tian, J.; Liu, Q.; Cheng, N.; Asiri, A. M.; Sun, X. *Angew. Chem., Int. Ed.* **2014**, *53*, 9577−9581. (h) Gao, M.-R.; Liang, J.-X.; Zheng, Y.-R.; Xu, Y.-F.; Jiang, J.; Gao, Q.; Li, J.; Yu, S.-H. *Nat. Commun.* **2015**, *6*, 5982. (i) Tian, J.; Cheng, N.; Liu, Q.; Xing, W.; Sun, X. *Angew. Chem., Int. Ed.* **2015**, *54*, 5493−5497.

(6) (a) Jaramillo, T. F.; Jorgensen, K. P.; Bonde, J.; Nielsen, J. H.; Horch, S.; Chorkendorff, I. *Science* **2007**, *317*, 100−102. (b) Lu, Z.; Zhang, H.; Zhu, W.; Yu, X.; Kuang, Y.; Chang, Z.; Lei, X.; Sun, X. *Chem. Commun.* **2013**, *49*, 7516−7518. (c) Lu, Z.; Zhu, W.; Yu, X.; Zhang, H.; Li, Y.; Sun, X.; Wang, X.; Wang, H.; Wang, J.; Luo, J.; Lei, X.; Jiang, L. *Adv. Mater.* **2014**, *26*, 2683−2687. (d) Vrubel, H.; Hu, X. *Angew. Chem., Int. Ed.* **2012**, *51*, 12703−12706. (e) Cao, B.; Veith, G. M.; Neuefeind, J. C.; Adzic, R. R.; Khalifah, P. G. *J. Am. Chem. Soc.* **2013**, *135*, 19186−19192.

(7) Yan, Y.; Xia, B.; Xu, Z.; Wang, X. *ACS Catal.* **2014**, *4*, 1693−1705.

(8) (a) Zhang, J.; Hao, J.; Wei, Y.; Xiao, F.; Yin, P.; Wang, L. *J. Am. Chem. Soc.* **2010**, *132*, 14−15. (b) Fang, X.; Kögerler, P.; Furukawa, Y.; Speldrich, M.; Luban, M. *Angew. Chem., Int. Ed.* **2011**, *50*, 5212−5216. (c) Miras, H. N.; Yan, J.; Long, D.-L.; Cronin, L. *Chem. Soc. Rev.* **2012**, *41*, 7403−7430. (d) Du, D.-Y.; Yan, L.-K.; Su, Z.-M.; Li, S.-L.; Lan, Y.-Q.; Wang, E.-B. *Coord. Chem. Rev.* **2013**, *257*, 702−717. (e) Miras, H. N.; Vilà-Nadal, L.; Cronin, L. *Chem. Soc. Rev.* **2014**, *43*, 5679−5699.

(9) (a) Patel, A.; Narkhede, N. *Energy Fuels* **2012**, *26*, 6025−6032. (b) Brahmkhatri, V.; Patel, A. *Fuel* **2012**, *102*, 72−77. (c) Du, D.-Y.; Qin, J.-S.; Wang, T.-T.; Li, S.-L.; Su, Z.-M.; Shao, K.-Z.; Lan, Y.-Q.; Wang, X.-L.; Wang, E.-B. *Chem. Sci.* **2012**, *3*, 705−710.

(10) (a) Feng, D.; Gu, Z.-Y.; Li, J.-R.; Jiang, H.-L.; Wei, Z.; Zhou, H.-C. *Angew. Chem., Int. Ed.* **2012**, *51*, 10307−10310. (b) Zhou, H.-C.; Long, J. R.; Yaghi, O. M. *Chem. Rev.* **2012**, *112*, 673−674. (c) Li, M.; Li, D.; O'Keeffe, M.; Yaghi, O. M. *Chem. Rev.* **2014**, *114*, 1343−1370. (d) Lu, W.; Wei, Z.; Gu, Z.; Liu, T.; Park, J.; Park, J.; Tian, J.; Zhang, M.; Zhang, Q.; Gentle, T., III; Bosch, M.; Zhou, H.-C. *Chem. Soc. Rev.* **2014**, *43*, 5561−5593.

(11) (a) Jahan, M.; Liu, Z.; Loh, K. P. *Adv. Funct. Mater.* **2013**, *23*, 5363−5372. (b) Gong, Y.; Shi, H.-F.; Jiang, P.-G.; Hua, W.; Lin, J.-H. *Cryst. Growth Des.* **2014**, *14*, 649−657.

(12) Du, D.-Y.; Qin, J.-S.; Li, S.-L.; Su, Z.-M.; Lan, Y.-Q. *Chem. Soc. Rev.* **2014**, *43*, 4615−4632.

(13) (a) Nohra, B.; Moll, H. E.; Albelo, L. M. R.; Mialane, P.; Marrot, J.; Mellot-Draznieks, C.; O'Keeffe, M.; Biboum, R. N.; Lemaire, J.; Keita, B.; Nadjo, L.; Dolbecq, A. *J. Am. Chem. Soc.* **2011**, *133*, 13363−13374. (b) Rousseau, G.; Rodriguez-Albelo, L. M.; Salomon, W.;

DOI: 10.1021/jacs.5b02688
J. Am. Chem. Soc. 2015, 137, 7169−7177

Mialane, P.; Marrot, J.; Donngmene, F.; Mbomekallé, I.; de Oliveira, P.; Dolbecq, A. *Cryst. Growth Des.* **2015**, *15*, 449−456.
(14) Mialane, P.; Dolbecq, A.; Lisnard, L.; Mallard, A.; Marrot, J.; Sécheresse, F. *Angew. Chem., Int. Ed.* **2002**, *41*, 2398−2401.
(15) (a) Dolbecq, A.; Mialane, P.; Lisnard, L.; Marrot, J.; Sécheresse, F. *Chem.—Eur. J.* **2003**, *9*, 2914−2920. (b) Dolbecq, A.; Mellot-Draznieks, C.; Mialane, P.; Marrot, J.; Férey, G.; Sécheresse, F. *Eur. J. Inorg. Chem.* **2005**, 3009−3018. (c) Rodriguez-Albelo, L. M.; Ruiz-Salvador, A. R.; Sampieri, A.; Lewis, D. W.; Gómez, A.; Nohra, B.; Mialane, P.; Marrot, J.; Sécheresse, F.; Mellot-Draznieks, C.; Biboum, R. N.; Keita, B.; Nadjo, L.; Dolbecq, A. *J. Am. Chem. Soc.* **2009**, *131*, 16078−16087. (d) Rodriguez-Albelo, L. M.; Ruiz-Salvador, A. R.; Lewis, D. W.; Gómez, A.; Mialane, P.; Marrot, J.; Dolbecq, A.; Sampieri, A.; Mellot-Draznieks, C. *Phys. Chem. Chem. Phys.* **2010**, *12*, 8632−8639. (e) Wang, W.; Xu, L.; Gao, G.; Liu, L.; Liu, X. *CrystEngComm* **2009**, *11*, 2488−2493.
(16) (a) Chae, H. K.; Siberio-Pérez, D. Y.; Kim, J.; Go, Y.; Eddaoudi, M.; Matzger, A. J.; O'Keeffe, M.; Yaghi, O. M. *Nature* **2004**, *427*, 523−527. (b) Zheng, S.-T.; Wu, T.; Chou, C.; Fuhr, A.; Feng, P.; Bu, X. *J. Am. Chem. Soc.* **2012**, *134*, 4517−4520.
(17) He, W.; Li, S.; Yang, G.; Lan, Y.; Su, Z.; Fu, Q. *Chem. Commun.* **2012**, *48*, 10001−10003.
(18) (a) Du, D.; Qin, J.; Li, Y.; Li, S.; Lan, Y.; Wang, X.; Shao, K.; Su, Z.; Wang, E. *Chem. Commun.* **2011**, *47*, 2832−2834. (b) Du, D.; Qin, J.; Wang, C.; Liu, X.; Li, S.; Su, Z.; Wang, X.; Lan, Y.; Wang, E. *J. Mater. Chem.* **2012**, *22*, 21040−21044.
(19) Delgado-Friedrichs, O.; O'Keeffe, M.; Yaghi, O. M. *Acta Crystallogr.* **2006**, *A62*, 350−355.
(20) (a) Dybtsev, D. N.; Chun, H.; Kim, K. *Chem. Commun.* **2004**, 1594−1595. (b) El-Kaderi, H. M.; Hunt, J. R.; Mendoza-Cortés, J. L.; Côté, A. P.; Taylor, R. E.; O'Keeffe, M.; Yaghi, O. M. *Science* **2007**, *316*, 268−272.
(21) Jiang, H.-L.; Makal, T. A.; Zhou, H.-C. *Coord. Chem. Rev.* **2013**, *257*, 2232−2249.
(22) Su, S.; Wang, S.; Song, X.; Song, S.; Qin, C.; Zhu, M.; Hao, Z.; Zhao, S.; Zhang, H. *Dalton Trans.* **2012**, *41*, 4772−4779.
(23) (a) Jiang, H.; Feng, D.; Wang, K.; Gu, Z.; Wei, Z.; Chen, Y.; Zhou, H. *J. Am. Chem. Soc.* **2013**, *135*, 13934−13938. (b) Du, D.; Qin, J.; Sun, Z.; Yan, L.; O'Keeffe, M.; Su, Z.; Li, S.; Wang, X.; Wang, X.; Lan, Y. *Sci. Rep.* **2013**, *3*, 2616.
(24) (a) Zhang, S.-M.; Chang, Z.; Hu, T.-L.; Bu, X.-H. *Inorg. Chem.* **2010**, *49*, 11581−11586. (b) Qin, J.-S.; Du, D.-Y.; Li, W.-L.; Zhang, J.-P.; Li, S.-L.; Su, Z.-M.; Wang, X.-L.; Xu, Q.; Shao, K.-Z.; Lan, Y.-Q. *Chem. Sci.* **2012**, *3*, 2114−2118.
(25) (a) Xing, Z.; Liu, Q.; Asiri, A. M.; Sun, X. *Adv. Mater.* **2014**, *26*, 5702−5707. (b) Liao, L.; Wang, S.; Xiao, J.; Bian, X.; Zhang, Y.; Scanlon, M. D.; Hu, X.; Tang, Y.; Liu, B.; Girault, H. H. *Energy Environ. Sci.* **2014**, *7*, 387−392.
(26) (a) Ernst, F. O.; Bchel, R.; Strobel, R.; Pratsinis, S. E. *Chem. Mater.* **2008**, *20*, 2117−2123. (b) Gu, M.; Li, Y.; Li, X. L.; Hu, S. Y.; Zhang, X. W.; Xu, W.; Thevuthasan, S.; Baer, D. R.; Zhang, J. G.; Liu, J.; Wang, C. M. *ACS Nano* **2012**, *6*, 8439−8447.
(27) Bo, X.; Zhu, L.; Wang, G.; Guo, L. *J. Mater. Chem.* **2012**, *22*, 5758−5763.
(28) Qian, L.; Yang, X. R. *Electrochem. Commun.* **2005**, *7*, 547−551.
(29) Cheng, L.; Zhang, X. M.; Xi, X. D.; Dong, S. J. *J. Electroanal. Chem.* **1996**, *407*, 97−103.
(30) Keita, B.; Belhouari, A.; Nadjo, L.; Contant, R. *J. Electroanal. Chem.* **1995**, *381*, 243−250.
(31) (a) Xie, J.; Zhang, H.; Li, S.; Wang, R.; Sun, X.; Zhou, M.; Zhou, J.; Lou, X. W.; Xie, Y. *Adv. Mater.* **2013**, *25*, 5807−5813. (b) Wang, T.; Liu, L.; Zhu, Z.; Papakonstantinou, P.; Hu, J.; Liu, H.; Li, M. *Energy Environ. Sci.* **2013**, *6*, 625−633.
(32) Li, Y. G.; Wang, H. L.; Xie, L. M.; Liang, Y. Y.; Hong, G. S.; Dai, H. J. *J. Am. Chem. Soc.* **2011**, *133*, 7296−7299.
(33) (a) Tran, P. D.; Nguyen, M.; Pramana, S. S.; Bhattacharjee, A.; Chiam, S. Y.; Fize, J.; Field, M. J.; Artero, V.; Wong, L. H.; Loo, J.; Barber, J. *Energy Environ. Sci.* **2012**, *5*, 8912−8916. (b) Kong, D.; Wang, H.; Cha, J. J.; Pasta, M.; Koski, K. J.; Yao, J.; Cui, Y. *Nano Lett.* **2013**, *13*, 1341−1347. (c) Youn, D. H.; Han, S.; Kim, J. Y.; Kim, J. Y.; Park, H.; Choi, S. H.; Lee, J. S. *ACS Nano* **2014**, *8*, 5164−5173.
(34) Hinnemann, B.; Moses, P. G.; Bonde, J.; Jørgensen, K. P.; Nielsen, J. H.; Horch, S.; Chorkendorff, I.; Nørskov, J. K. *J. Am. Chem. Soc.* **2005**, *127*, 5308−5309.
(35) Guo, C.; Zhang, L.; Miao, J.; Zhang, J.; Li, C. M. *Adv. Energy Mater.* **2013**, *3*, 167−171.
(36) (a) Sheldrick, G. M. *SHELXS-97, Programs for X-ray Crystal Structure Solution*; University of Göttingen: Göttingen, Germany, 1997. (b) Sheldrick, G. M. *SHELXL-97, Programs for X-ray Crystal Structure Refinement*; University of Göttingen: Göttingen, Germany, 1997. (c) Farrugia, L. J. *WINGX, A Windows Program for Crystal Structure Analysis*; University of Glasgow: Glasgow, UK, 1988.
(37) van der Sluis, P.; Spek, A. L. *Acta Crystallogr., Sect. A* **1990**, *46*, 194−201.
(38) Luo, W.; Yang, Z.; Li, Z.; Zhang, J.; Liu, J.; Zhao, Z.; Wang, Z.; Yan, S.; Yu, T.; Zou, Z. *Energy Environ. Sci.* **2011**, *4*, 4046−4051.

DOI: 10.1021/jacs.5b02688
J. Am. Chem. Soc. 2015, 137, 7169−7177